Available online at www.sciencedirect.com
SCIENCE DIRECT
International Journal of Mass Spectrometry 253 (2006) 181–192
International Journal of Mass Spectrometry
www.elsevier.com/locate/ijms

Fragmentation at and above surfaces in SIMS: Effects of biomolecular yield enhancing surface modifications

Stefan L. Luxembourg, Ron M.A. Heeren *

FOM Institute for Atomic and Molecular Physics, Kruislaan 407, 1098 SJ Amsterdam, The Netherlands

Received 29 September 2005; received in revised form 30 November 2005; accepted 28 December 2005
Available online 10 February 2006

Abstract

Matrix-enhanced SIMS and metal-assisted SIMS are successfully employed to increase the organic ion yield in SIMS. In this study we compare kinetic energy distributions obtained for the SIMS, ME-SIMS and MetA-SIMS sputtering of molecular ions. In comparison to the SIMS kinetic energy distributions, those obtained for ME-SIMS display larger energy deficits, indicative of entrainment of analyte ions by matrix molecules or collisions taking place above the sample surface. In the case of MetA-SIMS high energy broadening of the distributions is observed, resulting from the high stopping power of the gold used. A selection of substituted benzylpyridinium salts is used to investigate the effect of internal energy reduction in ME-SIMS. Kinetic energy distributions were used to separate the daughter ions formed in the sample region from those resulting from unimolecular decay on nanosecond timescales, in the first tens of micrometers above the sample surface. The longer-timescale decay was monitored by changing the energy acceptance window of the mass spectrometer used. From the decay rate constants internal energies of the precursor ions decaying on nanosecond timescales were determined using RRKM theory. Within the framework of the precursor model the results indicate an extension of the collision cascade over a wider area than in SIMS.

Keywords: Matrix-enhanced SIMS; Metal-assisted SIMS; Kinetic energy distribution; Internal energy; Precursor model

1. Introduction

The analysis of the biochemical content of cells is an exciting and challenging application for secondary ion mass spectrometry (SIMS). Its chemical specificity combined with its high lateral resolution make imaging SIMS a valuable addition to the palette of experimental tools for in life sciences.

Over the past years many reports have appeared on the elemental analysis of biological samples using dynamic SIMS [1]. The high ion doses used induce extensive fragmentation of all organic molecules present in the sample. Therefore, the insights obtained are limited to the (distributions of) elements and small organic fragments only, all molecular information is lost. In static SIMS much lower ion doses are used, therefore it is better suited for the analysis of organic samples. Although fragmentation is still extensive, small intact molecules like cholesterol and informative fragments like the phosphocholine-headgroup can readily be detected [2]. Despite, the successes in the mapping of elements and small organics, one of the key factors that is limiting the wide scale application of SIMS to biological systems is the low ionization yields for functional biomolecules [3].

Currently, several strategies to improve the ionization yields of molecular species are explored. It has been shown that the use of polyatomic primary ion beams like SF_5^+, C_{60}^+, Au_n^+ and Bi_n^{m+} greatly enhances the ionization yields of small organic species compared to mono-atomic primary ions like Ga^+ and In^+ [4]. Though, reports on the analysis of real world samples using polyatomic primary ion beams are still limited, yielding mainly cholesterol and phospholipid signals [5]. A recent publication has shown that the application of polyatomic primary ions is promising for the analysis of small peptides from combinatorial libraries [6]. Besides innovations on the nature of the primary ion projectile, sensitivity enhancing effects of sample preparation are investigated as well. Sample metallization (or metal-assisted-SIMS (MetA-SIMS)) and matrix-enhanced SIMS (ME-SIMS) belong to this latter category. Sample metallization as a means to improve organic molecular ion yields was introduced by Linton et al. [7]. Recently, it was shown that by

* Corresponding author. Tel.: +31 20 6081234; fax: +31 20 6684106.
E-mail address: heeren@amolf.nl (R.M.A. Heeren).

1387-3806/$ – see front matter © 2006 Elsevier B.V. All rights reserved.
doi:10.1016/j.ijms.2005.12.048

evaporating a minute layer of gold or silver onto organic samples among which polyalanine and polystyrene the ionization yields and efficiencies of the molecular ions were significantly improved, by at least an order of magnitude [8]. The enhancing effects in MetA-SIMS are not limited to the formation of metal-cationized pseudo-molecular ions only; the yield of protonated ions is improved as well. It has been shown that migration of organic species on to formed gold islands in combination with the increased stopping power of gold is a possible explanation for the sensitivity enhancement [8,9]. In this way the application of an overlayer of gold or silver is comparable to the use of a gold or silver substrate [10]. MetA-SIMS studies of tissue demonstrate that distributions of small biomolecules such as cholesterol (*m/z* 385) can be imaged effectively in this way [11,12]. Higher mass signals (800–1300 *m/z*) have been used to image different regions of single neuroblastoma cells [11]. The sensitivity enhancing effect of the presence of a matrix in which labile analyte ions are imbedded has been known for a longer period. Reduction of fragmentation in the presence of a solid matrix was recognized already in the eighties of the past century [13]. Recently, in the slipstream of the success of matrix-assisted laser desorption ionization (MALDI), the dissolvation of the analyte compounds in a matrix has received renewed attention. Wu and Odom [14] adopted the MALDI sample preparation protocol to record mass spectra of proteins with masses larger than 10 kDa. In these ME-SIMS experiments a dried-droplet sample preparation protocol was followed. As was shown in a recent publication [15], this results in an inhomogeneous sample, with locally varying ionization conditions. This kind of sample preparation is not favorable in an imaging experiment. For ME-SIMS imaging experiments on biological systems electrospray deposition (ESD) of the matrix is better suited. The first ME-SIMS imaging results using ESD have been published recently. In this study biomolecules from the nervous tissue of the pond snail *Lymnea Stagnalis* were mapped with 2.6 μm lateral resolution [16]. The molecular ion yield enhancement that is provided by the matrix in ME-SIMS has been attributed to several factors, which resemble the function of the matrix in MALDI. The presence of the matrix promotes molecular ion yields through ionization enhancement and fragmentation reduction. The acidic nature of the MALDI matrix promotes the formation of $[M+H]^+$ ions through proton donation [14]. The isolation of the analyte molecules by the matrix promotes desorption of large molecules through disentanglement of long organic molecular chains [17]. The lower degree of fragmentation in ME-SIMS has been observed on several occasions [14,15,18]. It has been attributed to a nestle environment for the analyte molecules provided by the solid matrix [14] and internal energy reduction through the desolvation of collectively desorbed matrix–analyte clusters. In MetA-SIMS reduced fragmentation has been observed as well [19].

In this study we have used a group of substituted benzylpyridinium (BPY) salts to investigate the reduction of fragmentation in ME-SIMS. The benzylpyridinium salts are so-called thermometer molecules; upon activation they undergo a simple C–N cleavage (Fig. 1), the activation energies of the different BPY precursor ions are known from quantum chemical calculations

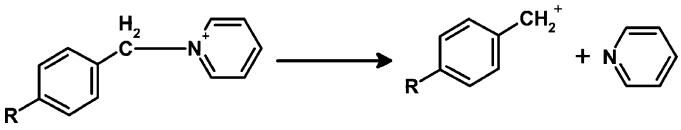

Fig. 1. Unimolecular decay of a *para*-substituted benzylpyridinium precursor ion by cleavage of the C—N bond. The activation energy for the reaction is dependent on the identity of the R-group.

and vary with the identity of the substituted side-group (second column, Table 1). Moreover, they are preformed ions in solution; if we assume that the BPYs retain this charge state in solution charge transfer can be excluded to play a role in any observed molecular ionization yield enhancement. In addition, since the size of the BPY precursor ions is comparable to the organic matrix molecules used in this study (2,5-dihydroxy benzoic acid) the mentioned isolation effect is eliminated as well. We have determined precursor ion yields and kinetic energy distributions (KEDs) for the BPY daughter and precursor ions. In this study a time-of-flight mass spectrometer equipped with electrostatic analyzers was used. The formation of BPY daughter ions was recorded at different instances along the ions' flight paths. In the acceleration region, in-sample formation of daughter ions was separated from nanosecond-timescale decay reactions taking place just above the sample surface. From the daughter ions' KEDs the associated decay rate constants were determined. The ions that decay at these early times make up the high internal energy tail of the sputtered precursor ion distributions. Rice-Ramsperger-Kassel-Marcus (RRKM) theory was used to estimate average internal energies of these rapidly decaying ions. Under normal operation conditions the BPY precursor ions decaying on μs timescales are not observed. This is due to the limited energy acceptance window of the mass spectrometer used. A method is presented to analyze these metastable ions. KEDs of peptide ions formed through the addition of H^+ or Na^+ and of the BPY preformed ions are compared. Furthermore, we have started a study on MetA-SIMS; first KED results are included as well. We have related our findings from the SIMS, ME-SIMS and MetA-SIMS KEDs to results from molecular dynamics simulations of the SIMS sputtering process of organic samples [17,20]. The observed decay of the precursor ions is discussed within the framework of Benninghoven's precursor model [21], which describes the dissipation of energy in the collision cascade around the point of impact of the primary ion.

Table 1
Activation energies of the different BPY variants

R	E_a (eV)	Precursor ion mass (Da)	Extraction potential (V)	t_{ESA1} (μs)
p-OCH_3	1.55	200	4600	11.4
p-Cl	2.04	204	4550	11.6
p-F	2.05	188	4675	10.9
p-CN	2.38	195	4675	11.1

The ions' masses and the extraction potentials were used in the SIMION simulations (see text). The daughter ions' masses are 79 Da lower. t_{ESA1} is the precursor ion flight time until the entrance of the first ESA. The flight times were determined in the SIMION.

2. Experimental

2.1. Materials and sample preparation

In this study we used a variety of samples and sample preparation methodologies. The thin layer samples were prepared by deposition of a 10 μl droplet of the solution containing the analyte onto a Si-wafer, which was then spin-coated for 1 min at 4000 rpm. The gold-coated samples were prepared by depositing a 10 μl droplet on a Si wafer, which was allowed to dry. Subsequently, a 1 nm gold layer was deposited using a Quorum Technologies (Newhaven, East Sussex, UK) SC7640 Sputter Coater. The ESD samples were obtained by premixing the analyte and matrix solutions to get the desired molar ratio. The matrix used in this study was 2,5-dihydroxybenzoic acid (DHB). The matrix–analyte mixture was then applied to a Si-wafer by ESD, using a home-built electro spray device [16]. The spray needle was kept at 4 kV, while the sample plate was grounded. The flow rate of the sprayed solution was set at 6 μl per hour, the spray was allowed to continue for approximately 40 min. All ESD samples were prepared at a matrix-to-analyte ratio of 2000:1. The analytes used in this study were a series of substituted benzylpyridinium and the small peptide Leucine Enkephalin. The DHB and the peptides were all purchased from Sigma–Aldrich (Germany). The benzylpyridinium salts used in this study are all *para*-substituted forms: *para*-chloro (*p*-Cl), *para*-fluoro (*p*-F), *para*-methoxy (*p*-OCH_3) and *para*-cyano (*p*-CN). The activation energies of the BPY precursor ions used are included in Table 1. The benzylpyridinium salts solutions (10^{-4} M, acetonitrile:water 1:1, v/v) were prepared at Liège University [22].

2.2. Mass spectrometry

All experiments described in this work were performed on a Physical Electronics (Eden Prairie, MN) TRIFT-II Time-of-Flight SIMS (TOF-SIMS) [23] equipped with an $^{115}In^+$ liquid metal ion gun. The spectra and KEDs shown in this paper were obtained using 15 keV primary ions (impact energy ~ 12 keV) in 12 ns long ion bunches of 1.5 nA dc ion current, which were compressed to 1 ns ion packages at the sample. Secondary ions were extracted through a 3.2 kV electric field into the TOF analyzer and post-accelerated by an additional 6 kV prior to detection on a dual multichannel plate phosphor screen detector. A multistop time-to-digital converter with 138 ps time resolution was used to acquire the detector signals. Mass resolution is optimized through time focusing of the secondary ions using three hemispherical electrostatic sector analyzers (ESAs). For analysis of the fragmentation products formed in the field free region of the mass spectrometer different source conditions were used (see below).

2.3. Kinetic energy distributions

Kinetic energy distributions are a valuable tool to experimentally study the fundamentals of the sputtering process. The KEDs give insight in the kinetic energy of the sputtered species; besides, characteristics of the formation and decay processes of the generated ions can be derived from observed energy deficits from the accelerating field energy (see below). The KEDs shown in this work were obtained in a way very similar as described before by Delcorte and Bertrand [24]. In short, the TRIFT ToF-mass spectrometer ion optics were tuned such that the secondary ions were maximally dispersed according to their kinetic energy just in front of the second ESA (Fig. 2). By moving a slit into the flight paths of the secondary ions, only the ions of a well-defined kinetic energy are allowed to pass. The width of the slit determines the energy resolution of the experiment. For this purpose we designed an adjustable slit, capable of slit widths between 50 μm and 1 mm, which could be moved in and out of the secondary ion pathways. All experiments described here were performed with the slit width set at 100 μm, corresponding to a 1.7 eV energy passband. The energy filter was stepped through the secondary ion pathways to record ion intensities at different kinetic energies resulting in KEDs. The translational step size of the filter was varied for different parts of the KED; the smallest step size was 20 μm resulting in oversampling of the distribution to obtain high quality data. In order to prevent sample degradation a fresh sample area was targeted for every position of the energy slit. Multiple KED curves were averaged to minimize the effects of sample variation. The zero-kinetic energy point was determined from the KEDs recorded for atomic

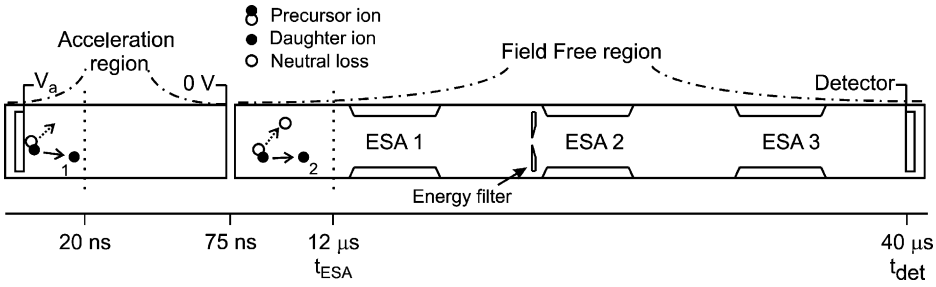

Fig. 2. A schematic representation of the TRIFT ToF mass spectrometer. The acceleration region and the field free drift region are indicated, immersion and transfer lenses are not included. The energy filter is located just in front of the second ESA. The axis below the schematics indicates the precursor ion flight time (or reaction time) at different stages. The daughter ion (1) that is formed from unimolecular decay in the acceleration region, taking place within the first 20 ns of its flight, is detected under normal operation conditions. Its rate of formation is estimated from the energy deficit part of its KED. The daughter ion (2), which is formed between the immersion lens and the entrance of the first ESA, is detected under elevated V_a conditions.

ions. It was taken as the crossing of the tangent of the decaying slope on the low energy side of the KED with the translation axis.

3. Unimolecular dissociation: theoretical and experimental considerations

On an instrument that is equipped with ESAs, like the TRIFT, precursor ions that fragment during their flight are largely not detected. This due to the limited kinetic energy acceptance window of the ESAs. The energy acceptance window under normal operation conditions was experimentally determined at 160 eV and the largest energy deficit that is still accepted at 80 eV. Upon decay of the precursor ion its kinetic energy (KE) is partitioned over the ionic fragment and neutral loss according to their respective masses. The kinetic energy of the daughter ions formed in the field free region, having acquired the full acceleration energy, follows from:

$$\frac{\Delta M}{M} \cdot \frac{E_k}{\Delta E_k} = 1 \tag{1}$$

where M and ΔM are the masses of the precursor ion and the neutral loss, respectively, and E_k and ΔE_k their kinetic energies. For a precursor ion of mass 200 Da (p-OCH_3), a neutral loss of 79 Da (pyridine) and an extraction potential of 3 kV, the daughter ions would have an energy deficit of approximately 1.2 keV and would not be detected. If the decay takes place in the acceleration region the precursor ions have not received their full acceleration yet. The location above the sample surface where the decay takes place determines the energy deficit from the accelerating field energy. Using Eqs. (2) and (3) (see next section) it can be shown that for the BPY precursor–daughter ion pairs only the daughter ions formed within the first 160 μm or 20 ns of their flight are detected. Fig. 2 illustrates the areas of the TRIFT mass spectrometer where daughter ion formation can be monitored.

3.1. Unimolecular dissociation in the acceleration region

The daughter ions observed in the SIMS mass spectrum arise from decay reactions taking place above the sample surface and from in-sample fragmentation. Ions formed above the sample surface will experience an energy deficit from the full acceleration energy; they will appear at negative apparent kinetic energy in the KED. The ratio between the areas under the negative and positive apparent kinetic energy parts of the KED curve can be used to separate the two contributions to the total daughter ion intensity.

The rate constant for the nanosecond-timescale decay of BPY precursor ions can be obtained from the energy deficit part of the daughter ion KED. The method used was adopted from Delcorte and Bertrand [25]. For clarity the derivation is included here. The energy deficit (E_d) is related to the position of fragmentation (x_d) by:

$$E_d = \frac{e \cdot V_a \cdot \Delta M}{d \cdot M} \cdot x_d \tag{2}$$

where d is the length of the acceleration region ($d = 2.1$ mm), V_a the acceleration potential, e the elemental charge, M and ΔM are the mass of the precursor and the neutral loss, respectively. The time and position of fragmentation are related through the equations of motion of the precursor ions in the acceleration region. Therefore, the time of fragmentation can be expressed in terms of the energy deficit:

$$\tau_f = C \cdot \sqrt{E_d} \tag{3}$$

with

$$C = \frac{M \cdot d}{e \cdot V_a} \cdot \sqrt{\frac{2}{\Delta M}} \tag{4}$$

A daughter ion KED is constructed of the daughter ion intensity (I_f) within an energy window around a given apparent KE, plotted against the apparent KE. In other words it corresponds to $\Delta I_f/\Delta E_k$, where E_k denotes the apparent KE. From the theory on unimolecular decay the time derivative of the daughter ion intensity is known to be:

$$\frac{dI_f}{dt} = k \cdot I_0 e^{-kt} \tag{5}$$

which is related to the experimentally obtained quantity through:

$$\frac{\Delta I_f}{\Delta E_d} \approx \frac{dI_f}{dE_d} = \frac{dI_f}{dt} \cdot \frac{dt}{dE_d} \tag{6}$$

Combination of Eq. (3)–(5) gives:

$$\frac{dI_f}{dE_d} = \frac{k_a \cdot I_0 \cdot C}{2 \cdot \sqrt{E_d}} \cdot e^{-k_a \cdot C \cdot \sqrt{E_d}} \tag{7}$$

After integration over dE_d:

$$I_f(E_d) = I_0 \cdot (1 - e^{-k_a \cdot C \cdot \sqrt{E_d}}) \tag{8}$$

from which the decay rate, k_a, is obtained from a fit to a mono-exponential function.

The decay rate constant that is obtained in this way is used to estimate the average internal energy of the ions in the high

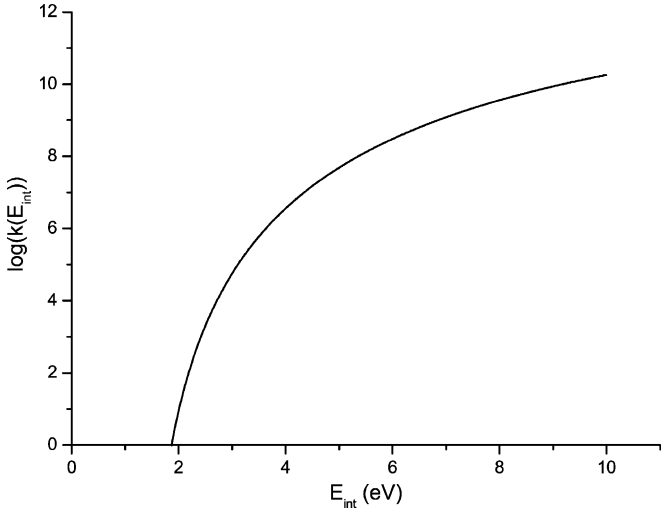

Fig. 3. An example of a decay rate vs. internal energy curve calculated according to RRKM theory. This particular curve was calculated for the p-OCH_3 substituted BPY.

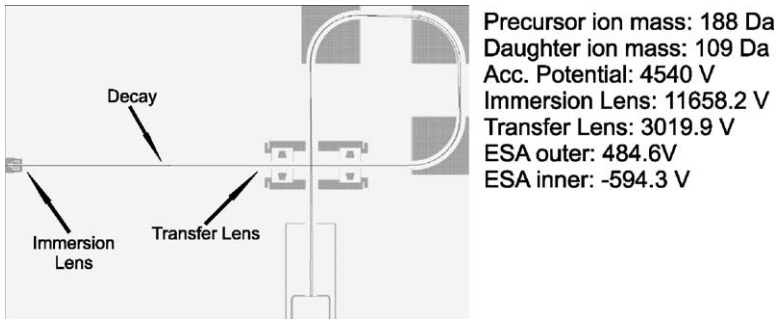

Fig. 4. The decay of *p*-F (*m*/*z* 188) precursor ions 5 μs after sputtering, the settings on the right guarantee transmission of the *m*/*z* 109 daughter ion.

internal energy tail of the sputtered precursor ion distribution. For this purpose the theoretical dependence of the rate constants on the internal energy was calculated using MassKinetics Scientific Demo software [26,27]. Fig. 3 contains an example of a rate constant versus internal energy curve.

3.2. Unimolecular dissociation in the field free region

The metastable BPY precursor ions that decay on microsecond timescales are not observed in the mass spectrum under standard experimental conditions. In order to study the slow metastable decay of the BPY ions the kinetic energy of their fragment ions has to be moved into the energy acceptance window of the mass spectrometer. Increasing the accelerating field and leaving the ESAs set for the acceptance of 3 keV ions achieves this. The accelerating potentials used to achieve this for the different BPYs are listed in Table 1. The ions that have not decayed when they reach the first ESA will collide with the electrodes because of their high kinetic energy. SIMION [28] simulations of the whole TRIFT mass spectrometer for metastable ions that decay in the field free region between the extraction plate and the first ESA spectrometer were performed at ULVAC-PHI. These simulations demonstrate that our approach to study metastable decay in the TRIFT is feasible. Fig. 4 contains the simulated ion trajectory for an *m*/*z* 188 ion (*p*-F), which decays 5 μs after it had been sputtered of the surface. The *m*/*z* 109 daughter ion reaches the detector, the settings used in the simulation are indicated on the right in the figure. The immersion lens is tuned for operation at high extraction potential while the transfer lens and ESAs are set for the normal extraction voltage. From the simulations it was found that ions that fragment inside the transfer lens are not detected (Fig. 5). In Table 1 the time interval during which metastable daughter ions become traceable in this way is included.

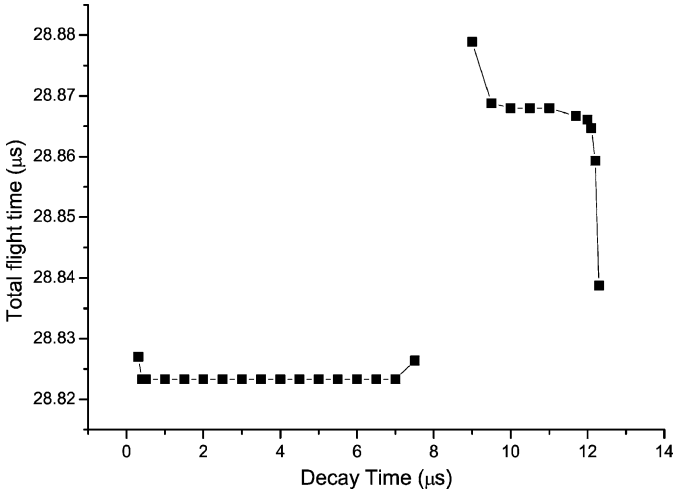

Fig. 5. Relation between the full daughter ion flight time and the instant of fragmentation. The gap in the curve corresponds to decay taking place inside the transfer lens, which results in a blind spot in the analysis of daughter ion formation.

4. Results

4.1. Mass spectra

The mass spectra obtained for the BPY salt samples were dominated in the 'high mass' region by the precursor (Py^+F) and daughter (F^+) ions produced through C–N bond scission, accompanied by DHB related peaks in the presence of matrix in the sample. As pointed out in the previous sections, the daughter ions observed in the mass spectrum of a standard SIMS, ME-SIMS or MetA-SIMS experiment are produced in the sample region and just above it. Besides the precursor–daughter ion pair also mass peaks that are indicative of hydrogen or H_2 loss were observed. These ions were formed in the sample region/source region and partly from metastable decay in the field free drift region. As the mass difference from the precursor ion is very small, ions produced from hydrogen loss in the field free spectrometer region can be detected (Eq. (1)). Small, non-specific organic fragments from the matrix and BPY species dominate the low mass region of the spectrum. These fragments are produced through energetic collisions taking place in the dense region of the collision cascade surrounding the position of impact of the primary ion.

4.2. Ion yields

The ion yield (*Y*) for a specific ion is defined as the number of detected secondary ions per primary ion. In Table 2, the ion yields that were determined for the BPY samples prepared according to the ESD and thin layer protocols are shown. Especially, for the thin layer samples the spread in ion yields is very limited. It is apparent that the presence of the DHB matrix results in higher ion yields for all the BPY species studied. The yield

Table 2
Ion yields in SIMS and ME-SIMS for the different BPY precursor ions

R	Y_{SIMS} ($\times 10^{-9}$)	$Y_{ME\text{-}SIMS}$ ($\times 10^{-9}$)	$Y_{ME\text{-}SIMS}/Y_{SIMS}$
p-OCH_3	3.5	4.2	1.2
p-Cl	6	86.1	14.4
p-F	13.2	95.7	7.3
p-CN	6.7	17.6	2.6

The last column shows the yield enhancement.

enhancement factor, included in the last column, varies between 1.2 and 14. This variation in yield enhancement, depending on the analyte of interest has been observed before in ME-SIMS [18].

4.3. Kinetic energy distributions

4.3.1. Thin layer sample

The KEDs obtained from the thin layer sample for the different benzylpyridinium salts studied are very similar. All distributions have their maximum around 1.2 eV and have a FWHM of approximately 2 eV. The fragment and precursor distributions are very similar. As an example in Fig. 6A distributions of the precursor and fragment ions of the *p*-F substituted BPY salt are shown. For a good comparison of the distributions they are normalized on their maximum intensities. In Fig. 6B the normalized distributions are plotted on a logarithmic scale. From this latter representation it becomes clear that the greatest differences between the distributions are in the region of negative apparent kinetic energies. While in this region the precursor distribution quickly falls off the fragment distribution follows a much slower decay. An apparent negative kinetic energy is indicative of an energy deficit from the accelerating field energy, which can find its origin in several processes. First of all the ions might have been formed above the sample surface, through gas-phase reactions in a desorption plume or through evaporation from a micro-droplet or cluster, both of these processes are often used to describe ion formation in matrix-assisted laser desorption/ionization [29] (MALDI). Secondly, collisions in the desorption plume above the sample surface can result in a reduction of the ion's the kinetic energy. Since for the very low ion doses used in SIMS only very little material is sputtered in each cycle of the experiment it is very unlikely that gas-phase collisions, and therefore also gas-phase reactions will induce any observable effects. Finally, the ion can be formed upon fragmentation from its precursor, the precursor's translational energy will than be distributed proportionally over the resulting ionic and neutral fragment species. Since the benzylpyridinium ions are preformed and only the fragment ions display the energy deficit it is obvious that the observed effect is predominantly a consequence of decay in the source region.

4.3.2. ESD sample

Using the energy slit differences in the kinetic energy of ions with respect to the full acceleration field energy are detected. Therefore, it is crucial that the ions experience a constant accelerating field during the experiments; any effects of charging of the sample should be avoided. Sample charging is not expected to be a problem for the thin layer sample preparations, though when non-conductive samples like matrix crystal layers are studied it can be of significance. Although the ESD method was chosen to deposit the matrix–analyte mixture because it produces very homogeneous, thin layers of crystals. Taking into account the non-conductive character of the matrix crystal layer, distortion of the accelerating field is still likely to occur. To investigate the distorting effect on the KEDs, we monitored their evolution in time, during the course of an experiment. A change in the accelerating potential due to charging of the sample will shift the KED peak position with time. 3D-KED plots were calculated from RAW-files. In this file format intensity data, and flight times are stored in equal size data blocks, each block was provided with an acquisition time stamp. In this way the time resolution obtained in the 3D-KED is dependent on the signal intensity: high signal intensity fills up the data blocks relatively fast, resulting in relatively short time interval between subsequent time stamps. In this way the highest time resolution was obtained for the high intensity part of the KED. This made that for an interval of 4 eV around the peak position a time resolution of 250 ms was obtained. The 3D-KED plot for the *p*-OCH_3 BPY precursor is shown in Fig. 7. It becomes apparent there is a slight charging effect during the first 10 s of the experiment. The total effect is below 0.5 eV, which falls within our energy slit resolution. Therefore, it is concluded that this phenomenon

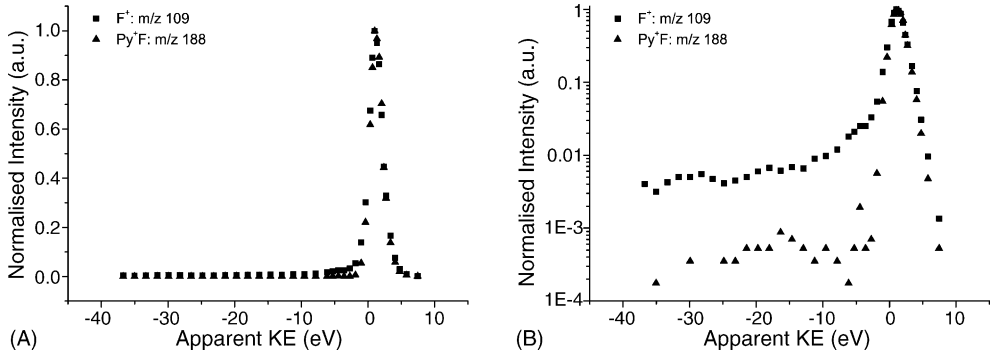

Fig. 6. Normalized KEDs of the precursor and daughter ions of the *p*-F BPY for a thin layer sample (A) shown for linear scales and (B) for logarithmic intensity scale to stress the observed differences. The daughter ion distribution is extended to negative apparent energies. The ions observed at negative apparent energies result from metastable decay in acceleration region above the sample surface.

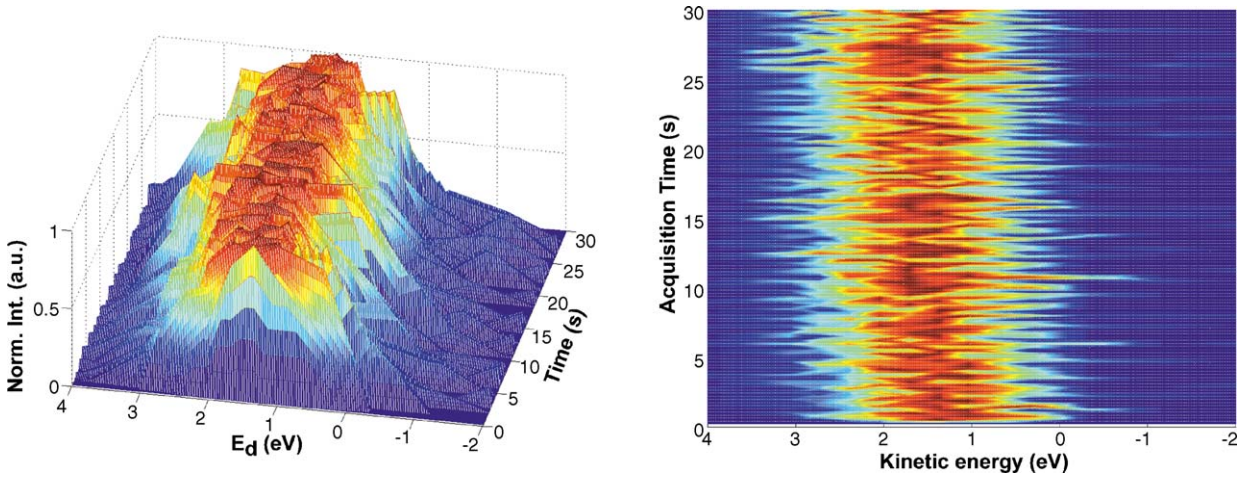

Fig. 7. Time resolved kinetic energy distributions for an ESD sample of the *p*-OCH_3 BPY precursor ion. In the first 10 s only a slight shift in the location of the maximum intensity is observed. Therefore, it is concluded that charging of the sample does not interfere with recording of KEDs on ESD samples.

will only have a marginal effect on the KEDs of ions created from an ESD matrix–analyte sample.

As for the case of the matrix-free samples the KEDs recorded for the different BPY salts demonstrated similar features. The distributions peak between 1.8 and 3 eV and the FWHM is around 3 eV. Fig. 8 contains the precursor and daughter ions KEDs obtained in an ME-SIMS experiment for the *p*-CN benzylpyridinium salt. Close examination of the curves tells us that the KED of the fragment ion is broadened towards the positive kinetic energy side with respect to that of the precursor. The positive KE part of the distribution comprises of ions that have gained KE in the collision cascade. Broadening of fragment distributions has been observed before [24]. Since, the precursor ions that are most likely to undergo fragmentation are the ones with the highest internal energy, the depletion of the high kinetic energy side of the precursor KED indicates that the ions that gain the most kinetic energy (∼4–5 eV) during the desorption process also receive a large amount of internal energy. In comparison to the matrix-free case the fall off of the fragment ion distribution with increasing energy deficit is less rapid, which is indicative of a slower decay rate. The precursor ion KED also displays some intensity at low energy deficits. To illustrate the inhomogeneous nature of the broadening of the precursor distribution (only to the negative apparent KE side) in comparison to the matrix-free situation we shifted the precursor KEDs, obtained for the *p*-F substituted BPY in SIMS and ME-SIMS, respectively, to make the peak positions overlap (see Fig. 9). It is apparent that in the presence of DHB the precursor distribution is broadened to the low (negative) apparent KE side only. Height differences in the sample can also be a source of broadening, though these would result in broadening on the positive as well as on the negative apparent KE sides of the distribution. Since the BPYs are preformed ions the energy deficit can be explained by a MALDI-like entrainment of the precursor ions by the dominating matrix molecules. Though since the amount of material removed in a ME-SIMS experiment is greater than in a SIMS experiment collisions in the region just above the sample surface can also be a source of energy deficit. KEDs obtained with MALDI (not shown) display much larger energy deficits, which shows that in ME-SIMS far less collisions are involved or that association extends over a much smaller area. For the hypothesis of association we can estimate the distance

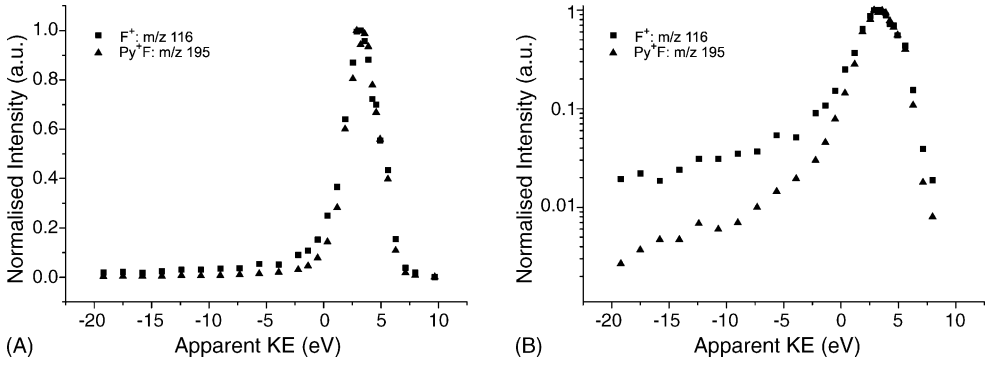

Fig. 8. Normalized KEDs of precursor and daughter ion pair of the *p*-CN substituted BPY obtained for an ESD sample (A) on linear scales and (B) on logarithmic intensity scale. For the ESD sample the precursor ion KED shows significant intensity at negative apparent KE, most likely this is caused by clustering with matrix molecules.

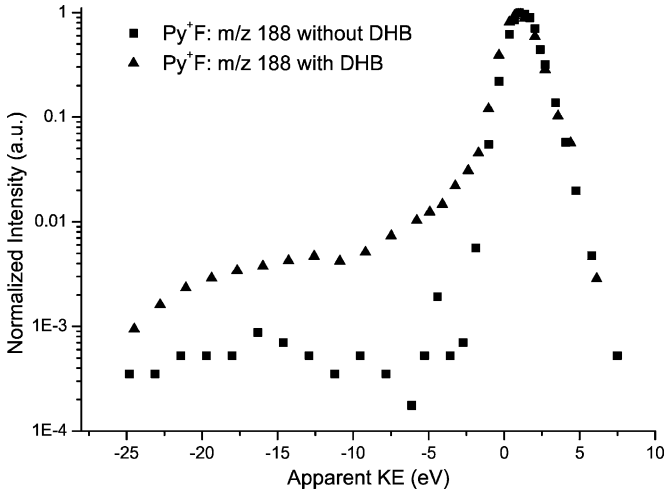

Fig. 9. The differences in the KEDs of the *p*-F BPY variant recorded on the thin layer sample and ESD sample are limited to the energy deficit part of the distribution.

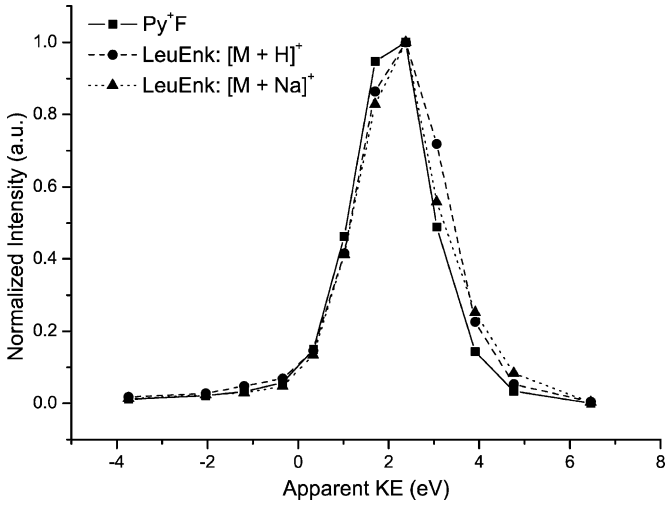

Fig. 10. KEDs of the precursor ion of the *p*-OCH_3 BPY and two pseudo-molecular ions of the peptide Leucine Enkephalin from an ESD sample. The addition reactions needed to form the pseudo-molecular peptide ions do not occur over an extended area. The higher kinetic side shows increased intensity for the peptide ions due to the increased degrees of freedom (see text).

and timescale over which this takes place from Eq. (2). To do so we have to make the assumption that the BPY precursor ions concerned are formed upon desolvation from clusters which are neutral or ionic with a high mass-to-charge ratio, e.g., containing multiple (matrix-) molecules. For these cases the kinetic energy obtained from the accelerating field is either zero or negligible. The initial velocities of the sputtered clusters lie in the range of 400–500 m/s [17]. Therefore, the initial kinetic energy of a desolvated BPY precursor ion, acquired during the desorption process, is negligible as well. The rapid fall off (∼4 eV) of the precursor ion distribution with increasing energy deficit points to a very narrow (≤3 μm) region above the sample surface, in which the BPY ions and organic matrix are associated. A recent molecular dynamics study [17] showed that entrainment of analytes in clusters of matrix molecules is likely at early times (≤100 ps) in the desorption process. For the quoted velocities of sputtered clusters the energy deficit we observe here would require the analyte and matrix molecules to remain associated for times on the order of several nanoseconds. Comparison of the mass spectra/time traces recorded for the thin layer and ESD sample revealed a ∼2 ns broadening to longer flight times for the latter one, in line with the entrainment hypothesis.

Fig. 10 shows KEDs that were recorded for an ESD sample containing both the *p*-OCH_3 BPY and the small peptide Leucine Enkephalin. In order to detect the peptide a protonation or cationization reaction has to take place. Comparison of the energy deficit tails of the KEDs of the preformed BPY precursor ions and the quasi-molecular peptide ions should give insight in the localization of this addition reaction. The negative tails KEDs of the quasi-molecular peptide ions and the benzylpyridinium ion overlap. Therefore, there is no reason to assume that the protonation or cationization occurs over an extended area above the sample surface. The broadening at the positive side of the peptide ion KEDs compared to the *m/z* 200 BPY precursor ion could be a size effect. The Leucine Enkephalin fragmentation threshold energy is higher; more internal energy can be stored in the molecule due to its many degrees of freedom. This explanation is in line with the view that the molecular ion undergoes multiple uncorrelated collisions before it is ejected from the sample. However, results from an MD study demonstrate that the ejection of molecular species by the correlated uplifting by multiple substrate atoms gives rise to a combination of low internal energy and high kinetic energy [10]. Thus, it can be argued that the observed broadening of the peptide ion KED is indicative of a relatively high amount of intact peptide ions produced from collective motions in the sample.

4.3.3. Gold-coated sample

In general the KEDs obtained for the 1 nm gold-coated benzylpyridinium sample display similar characteristics as the ones obtained for the ESD matrix sample. The features that result from the unimolecular decay of the precursor ion are apparent. The main difference with the ESD sample case is in the width of the distributions. The KEDs obtained for the gold-coated sample are much wider, 2.5 eV versus 4 eV for the precursor ion in the ME-SIMS and gold-SIMS case, respectively. This observation is illustrated in Fig. 11A and B where the *p*-OCH_3 precursor and daughter ion KEDs for the two sample preparation techniques are compared. The broadening of the distribution predominantly takes place at the high kinetic energy side. It has been observed before that KEDs for gold covered organic samples can extend up to 10 eV KE [8]. This behavior has been used to substantiate the similarities with thin layer organic samples on gold substrates. As mentioned above it has been shown in molecular dynamics studies that the correlated upward motion of multiple surface atoms can result in the uplifting of an organic molecule from the surface, with relatively low internal energy and high kinetic energy [10]. It was not possible to efficiently sputter peptide ions from a gold-coated sample. Recently, it has been shown that the sputtering of peptide ions of metallic surfaces (gold or silver) is more successful [30].

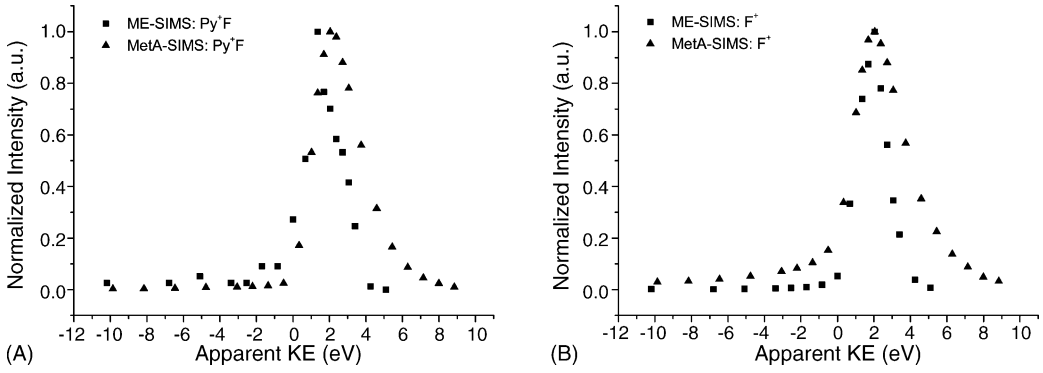

Fig. 11. Comparison of the MetA-SIMS and ME-SIMS KEDs for the *p*-OCH_3 BPY: (A) the precursor ions and (B) the daughter ions.

5. Decay rate constants, survival yields and internal energies

5.1. Daughter ion formation in the acceleration region

The rate constants for the fast decay of the BPY precursor ions in the source region of the instrument was deduced from the energy deficit part of the KED as was detailed in Section 3.1. With the substitution of Eq. (3), the mono-exponential growth function of Eq. (8) is transferred to the time-domain. Fig. 12 shows the result of the integration and substitution and the subsequent fitting procedure. All the decay rate constants, obtained in this way are included in Table 3. As was seen in the previous section, the precursor KEDs obtained for the ESD samples displayed some intensity at negative apparent energies, this was explained to arise from association of molecules/ions above the sample surface or collisions. Most likely, daughter ions formed in the sample region will be involved in these processes as well. To evaluate this effect on k_a we subtracted the KED of the *m/z* 154 molecular ion of DHB from the daughter ion KED (normalized on total area) and subsequently determined the effective rate constant. Since no large effects were observed, the numbers in Table 3 are obtained directly from the daughter ion KED. The uncertainties in the values of k_a obtained from the fitting procedure are all within 10% of numbers quoted. Therefore, all rate constants except the ones for the *p*-F and *p*-Cl variants in the ME-SIMS case can be readily distinguished. The ME-SIMS rate constants display a clear relation with the activation energies (Table 1), the higher the activation energy the lower the rate constant. From the SIMS results such a relation is not clear. Although below the peculiar nature of the *p*-Cl substituted BPY ion will be discussed, the result obtained for the *p*-CN substituted one is clearly an outlier. The rate constants determined on the ESD samples are without exception lower than the ones obtained for the thin layer sample. The average internal energy values of the ions in the 'hot' tail of the precursor ion distribution was derived from rate constant versus internal energy curves as in Fig. 3. The resulting energies are included in Table 3. We estimated the uncertainty in

Table 3
The rate constants for the decay of the BPY precursor ions in the first part of the acceleration region

R	k_a (s^{-1})	E_{int} (eV)	$I_f^A : I_f^S$
SIMS			
p-OCH_3	3×10^8	6.3	1:5.8
p-Cl	1.3×10^8	7.2	1:4.5
p-F	1.6×10^8	7.3	1:3.4
p-CN	2.7×10^8	9.5	1:2.6
ME-SIMS			
p-OCH_3	1.4×10^8	5.8	1:5.0
p-Cl	9.4×10^7	7.0	1:3.8
p-F	9.3×10^7	7.0	1:2.8
p-CN	6.6×10^7	8.4	1:4.6

The E_{int} values indicate an average internal energy of the decaying precursor ions.

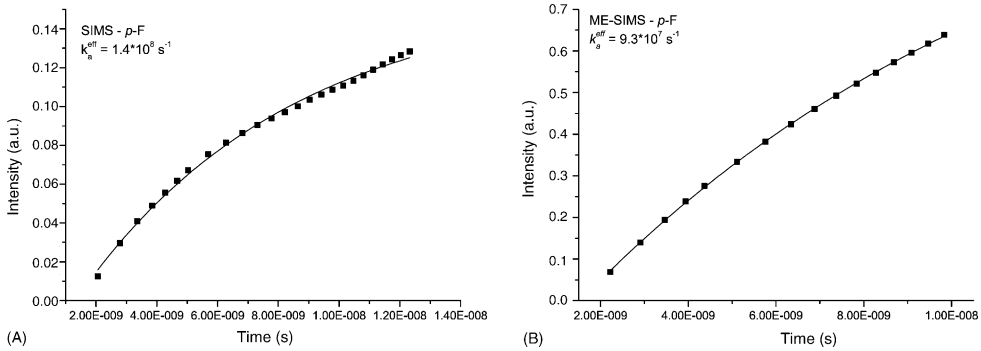

Fig. 12. The integrated energy deficit part of the KED of the daughter ions of the *p*-F BPY recorded in (A) SIMS and (B) ME-SIMS fit to a mono-exponential function.

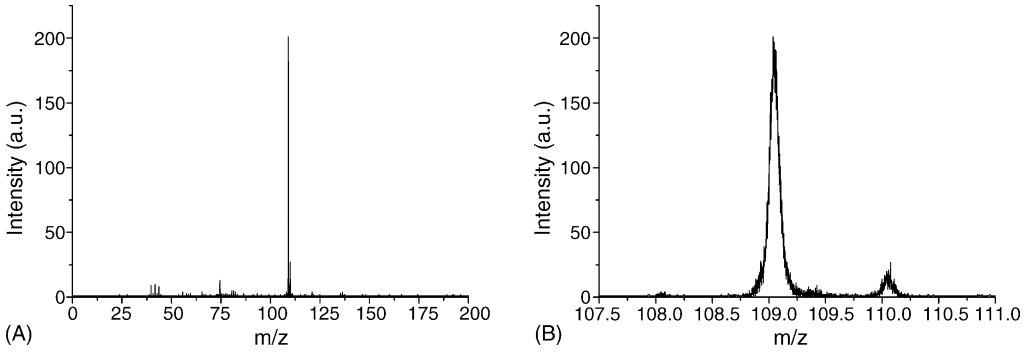

Fig. 13. (A and B) ME-SIMS metastable mass spectra of the *p*-F BPY daughter ion.

the internal energy values to be below 0.1 eV in all cases by projecting the uncertainty window around k_a onto the RRKM curve. Two observations can be made. First, the internal energy increases with higher activation energy and second the internal energies derived for ME-SIMS are without exception lower than for SIMS. The dependence of the internal energy values on the activation energy must result from an increased fragmentation at very early times ($<10^{-9}$ s) in the sample region. As a result the lower activation energy BPY ion populations have cooled down more. This should also be reflected in the ratio between in-sample (I_f^S) and above the sample fragmentation (I_f^A). The ratios are derived from the daughter ion KEDs as explained in Section 2. They are included in Table 3. All the $I_f^A : I_f^S$ ratios except the *p*-CN results advocate an increase of the ratio with lower threshold energy. On average the ratios found are higher for SIMS than for ME-SIMS. This implies that besides the nature of the sample also the activation energy is an important factor for in-sample fragmentation.

5.2. Daughter ion formation in the field free drift region

In Fig. 13A, a mass spectrum is shown that was obtained according to the protocol for the detection of metastable BPY ions decaying on μs timescale, described in Section 3.2. The spectrum was recorded on an ESD sample containing the *p*-F BPY salt. It is clear that the spectrum is dominated by the daughter ion; the precursor ion (*m/z* 188.09) is completely absent. Besides, some low signal intensity peaks are recorded at low *m/z* values. These most likely result from metastable decay of (hot) fragments formed in the sample region. They cannot be formed directly from the BPY precursor since the large mass difference would cause their kinetic energy to lie outside the acceptance window. Fig. 13B contains a zoom of the daughter ion region. Although the mass peaks are broader than in a normal SIMS acquisition, the fact that the mass resolution is around 1500 ($m/\Delta m$) indicates that the instrument's ESAs are still capable of time focusing the ions. Besides the outlined C–N scission another metastable decay mechanism was observed. In Fig. 14 the KEDs of the *para*-fluor substituted BPY precursor ion and the ions produced by the loss of one and two hydrogen atoms, respectively, are shown. The satellite peaks in the KEDs indicate metastable decay in the drift region with relatively small neutral loss (Eq. (1)). The energy deficits found for the *m/z* 187 and the *m/z* 186 ions match the loss of one hydrogen atom (∼15 eV). For the loss of H_2 an energy deficit of twice this value is requires, this was not observed (not shown), and therefore it was concluded that the *m/z* 186 ion is formed from two subsequent single hydrogen losses. To get an estimate of the fraction of the precursor ions, which decays according to this separate decay channel, the fragmentation, taking place in the source region and field free drift region was determined separately from the fragmentation taking place in the sample according to the method explained in the previous section. It was found that the C–N bond scission is by far the dominating pathway, approximately 5% of total fragmentation involves hydrogen loss.

The ratios of the intensities of the daughter ions formed in the field free drift region relative to the precursor ion intensity recorded under normal conditions are shown in third and fourth column of Table 4. Only the result for *p*-Cl is not in line with the expected trend of lower ratio for lower activation energy. In a very recent study that used benzylpyridinium ions to determine internal energy distributions in electrospray ionization the *para*-chloro substituted benzylpyridinium ion gave rise to a distribution that was clearly lower in energy than determined for other variants [27]. An explanation for this behavior might be

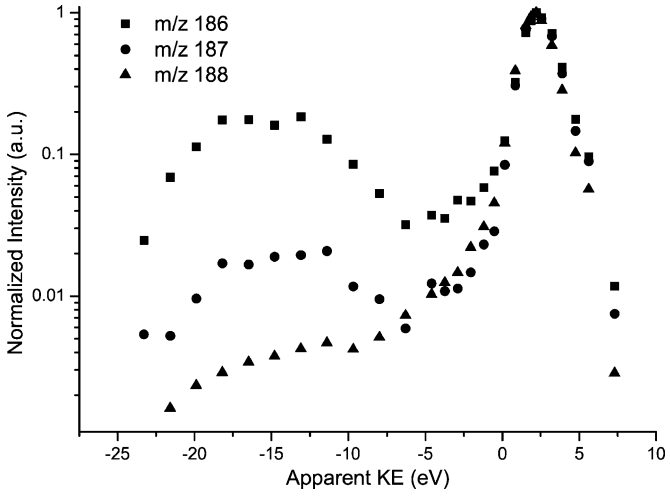

Fig. 14. KEDs for the *p*-F BPY precursor ions and two ions formed by the loss of one and two hydrogen atoms. From the location of the satellite peak the mass of the precursor ion can be determined according to Eq. (1) (see text).

Table 4
The intensities of daughter ions formed at different instances in the mass spectrometer relative to the precursor ion intensity

R	$I_f^S : I_P$	$I_f^A : I_P$	$I_{FF}:I_P$
SIMS—daughter ion formation			
p-OCH_3	9	1.5	1.5 ± 0.1
p-Cl	2.2	0.48	0.38 ± 0.06
p-F	2.2	0.64	0.43 ± 0.04
p-CN	1.4	0.55	0.33 ± 0.05
ME-SIMS—daughter ion formation			
p-OCH_3	2.2	0.44	0.56 ± 0.03
p-Cl	0.30	0.08	0.21 ± 0.05
p-F	0.35	0.13	0.30 ± 0.06
p-CN	0.30	0.07	0.25 ± 0.02

I_f^S is the intensity of daughter ions formed in the surface region, I_f^A of those formed in the first 20 ns of the flight and I_{FF} those formed between 300 ns and approximately 11 μs. An uncertainty of approximately 10% was estimated in the values for $I_f^S : I_P$ and $I_f^A : I_P$. To get to this estimate we assumed a 20% uncertainty in the values of I_f^S and I_f^A.

that its actual threshold energy is higher than determined from quantum chemical calculations.

6. Discussion and conclusions

The daughter ions formed at different instances during the ion's flight through the mass spectrometer (Fig. 2) have been determined. All daughter ion intensities obtained are shown relative to the precursor ion intensity in Table 4. The fragmentation increases with decreasing activation energy as expected, except for *p*-Cl. At every instance in the mass spectrometer the fragmentation in ME-SIMS is relatively lower than in SIMS, which is indicative of a cooler population of precursor ions. From the fast decay in the acceleration region we were able to determine an average internal energy value for the hottest ions that have escaped the sample surface. It is clear that the internal energy of the ions produced in SIMS extends to higher values. Although we have not recorded all the daughter ions formed, from the values in Table 4 it can readily be seen that in ME-SIMS the number of daughter ions formed per detected precursor is approximately four times lower than in SIMS. The difference between the relative amounts of fragments is the largest for the decay taking place in the sample region and in the acceleration region. According to Benninghoven's precursor model the energy profile $E(r)$ around the primary ion's impact point is described by a bell-shaped curve ($\sim 1/r^2$). The nature of the species ejected at different distances from the impact point mirrors the local energy density [31]. From this respect the precursor and daughter ions that were created at different instances in the mass spectrometer (sample, source region and field free drift region) can be thought to result from rims located at different distances from the point-of-impact. The changes in relative ratios between the intact precursor ions and the daughter ions formed at different flight times indicate that the outer rim area, where intact ions are produced from should be relatively larger in the case of ME-SIMS. This is achieved when the decrease in energy density is less rapid for an ESD sample, resulting in the collision cascade extending over a wider area. The disappearance cross-section, which is defined as the mono-exponential decay of the sputtered ion signal intensity with ion dose, is considered to be a good measure of the ejection radius of the sputtered ion [31]. Unpublished results on the disappearance cross-section of BPY ions with SIMS and ME-SIMS indicate a higher cross-section for the latter methodology, which is in line with the above. Results from molecular simulations show that energy can indeed diffuse better through a matrix containing bulk sample [17]. The energy deficits observed in the KEDs of the BPY precursor and Leucine Enkephalin ions can be explained in terms of a MALDI like internal energy reduction mechanism: desolvation of matrix–analyte clusters in the gas-phase, as suggested by several authors.

Clearly, the reduced fragmentation observed in ME-SIMS cannot fully explain the increase in ionization yields, presented in this study (Table 2) as well as in other studies [15,18]. Especially not since the analyte is present in 1:2000 ratio. The choice of BPY ions as analyte species excludes yield enhancing effects, like proton donation and analyte isolation to play an important role. Production of molecular ions from greater depths in the sample (as compared to the thin layer sample) will contribute to the higher molecular yield. Furthermore, segregation might concentrate the analyte ions in the near surface area [32]. Since SIMS analysis is limited to the first few monolayers of the sample, this would result in a lower matrix-to-analyte ratio for the part of the sample probed. An expanded area influenced by the collision cascade in ME-SIMS, as suggested here, does not only lead to a reduction of fragmentation but also to a larger amount of material being sputtered, which will increase the molecular ion yield further.

Acknowledgements

We would like to thank Jean-François Greisch from University Liège (Mass Spectrometry Lab) for the preparation of the BPY samples, Hideo Iwai of ULVAC-PHI Inc. for the SIMION ion trajectory simulations and Laszlo Drahos from the Hungarian Academy of Sciences (Mass Spectrometry Department) for his help with the calculation of the RRKM curves.

This work is part of research program nr. 49 "Mass spectrometric imaging and structural analysis of biomacromolecules" of the "Stichting voor Fundamenteel Onderzoek der Materie (FOM)", which is financially supported by the "Nederlandse organisatie voor Wetenschappelijk Onderzoek (NWO)".

References

[1] S. Chandra, G.H. Morrison, Int. J. Mass Spectrom. Ion Proc. 143 (1995) 161;
S. Chandra, D.R. Smith, G.H. Morrison, Anal. Chem. 72 (2000) 104A;
S. Chandra, Appl. Surf. Sci. 203 (2003) 679.
[2] D.M. Cannon Jr., M.L. Pacholski, N. Winograd, A.G. Ewing, J. Am. Chem. Soc. 122 (2000) 603;
S.G. Ostrowski, C.T.V. Bell, N. Winograd, A.G. Ewing, Science 305 (2004) 71;
T.P. Roddy, J. Cannon, M. Donald, S.G. Ostrowski, N. Winograd, A.G. Ewing, Anal. Chem. 74 (2002) 4020.
[3] R.M.A. Heeren, L.A. McDonnell, E. Amstalden, S.L. Luxembourg, A.F.M. Altelaar, S.R. Piersma, Appl. Surf. Sci., accepted for publication.

[4] F. Kollmer, Appl. Surf. Sci. 231–232 (2004) 153;
D. Weibel, S. Wong, N. Lockyer, P. Blenkinsopp, R. Hill, J.C. Vickerman, Anal. Chem. 75 (2003) 1754;
D.E. Weibel, N. Lockyer, J.C. Vickerman, Appl. Surf. Sci. 231–232 (2004) 146.
[5] D. Touboul, F. Hagland, A. Brunelle, R. Kersting, E. Tallarek, B. Hagenhoff, O. Laprevote, Anal. Chem. 76 (2004) 1550.
[6] J. Xu, C.W. Szakal, S.E. Martin, B.R. Peterson, A. Wucher, N. Winograd, J. Am. Chem. Soc. 126 (2004) 3902.
[7] R.W. Linton, M.P. Mawn, A.M. Belu, J.M. DeSimone, M.O. Hunt, Y.Z. Menceloglu, H.G. Cramer, A. Benninghoven, Surf. Interface Anal. 20 (1993) 991.
[8] A. Delcorte, J. Bour, F. Aubriet, J.-F. Muller, P. Bertrand, Anal. Chem. 75 (2003) 6875.
[9] A. Delcorte, N. Médard, P. Bertrand, Anal. Chem. 74 (2002) 4955.
[10] A. Delcorte, X.V. Eynde, P. Bertrand, J.C. Vickerman, B.J. Garrison, J. Phys. Chem. B 104 (2000) 2673.
[11] A.F.M. Altelaar, I. Klinkert, K. Jalink, R.P.J. de Lange, R.A.H. Adan, R.M.A. Heeren, S.R. Piersma, Anal. Chem. 78 (2006) 734.
[12] H. Nygren, P. Malmberg, C. Kriegeskotte, H.F. Arlinghaus, FEBS Lett. 566 (2004) 291.
[13] L.K. Liu, K.L. Busch, R.G. Cooks, Anal. Chem. 53 (1981) 109.
[14] K.J. Wu, R.W. Odom, Anal. Chem. 68 (1996) 873.
[15] S.L. Luxembourg, L.A. McDonnell, M. Duursma, X. Guo, R.M.A. Heeren, Anal. Chem. 75 (2003) 2333.
[16] A.F.M. Altelaar, J. van Minnen, C.R. Jimenez, R.M.A. Heeren, S.R. Piersma, Anal. Chem. 77 (2005) 735.
[17] A. Delcorte, B.J. Garrison, J. Phys. Chem. B 107 (2003) 2297.
[18] L. Adriaensen, F. Vangaever, J. Lenaerts, R. Gijbels, Rapid Commun. Mass. Spectrom. 19 (2005) 1017.
[19] L. Adriaensen, F. Vangaever, R. Gijbels, Anal. Chem. 76 (2004) 6777.
[20] A. Delcorte, B.J. Garrison, J. Phys. Chem. B 104 (2000) 6785.
[21] A. Benninghoven, Springer Verlag, Berlin, Germany, 1983.
[22] E.D. Pauw, G. Pelzer, P. Natalis, Springer Ser. Phys. 9 (1986) 103.
[23] B. Schueler, P. Sander, D.A. Reed, Vacuum 41 (1990) 1661;
B.W. Schueler, Microsc. Microanal. Microstruct. 3 (1992) 119.
[24] A. Delcorte, P. Bertrand, Nuclear Instruments & Methods in Physics Research Section B—Beam Interactions with Materials and Atoms 115 (1996) 246.
[25] A. Delcorte, P. Bertrand, Int. J. Mass. Spectrom. 184 (1999) 217.
[26] L. Dráhos, K. Vékey, J. Mass. Spectrom. 36 (2001) 237.
[27] J. Naban-Maillet, D. Lesage, A. Bossée, Y. Gimbert, J. Sztáray, K. Vékey, J.-C. Tabet, J. Mass. Spectrom. 40 (2005) 1.
[28] D.A. Dahl, Int. J. Mass Spectrom. 200 (2000) 3.
[29] M. Karas, D. Bachmann, U. Bahr, F. Hillenkamp, Int. J. Mass Spectrom. Ion Proc. 78 (1987) 53.
[30] S.L. McArthur, M.C. Vendettuoli, B.D. Ratner, D.G. Castner, Langmuir 20 (2004) 3704.
[31] A. Delcorte, B.G. Segda, B.J. Garrison, P. Bertrand, Nucl. Instrum. Methods B 171 (2000) 277.
[32] W. Szymczak, K. Wittmaack, Rapid Commun. Mass. Spectrom. 16 (2002) 2025.